GEOLOGICA CARPATHICA, 2026, 77, 6, 477–492 https://doi.org/10.31577/GeolCarp.2026.25

Early Permian A-type mylonitic granites of the northern Gondwana margin "Sanandaj–Sirjan Zone", Iran: Zircon U–Pb and Sr–Nd isotopic data

MAHSA TAHMASEBI[1], ALI A. SEPAHI[1,2,✉], MIRMOHAMMAD MIRI[3], JAVAD IZADYAR[4], CHRISTINA GÜNTER[5], JESÚS M. ANZANO[6] and JUAN BUIL-GARCÍA[6]

[1]Department of Geology, Faculty of Science, Bu-Ali Sina University, Hamedan, Iran
[2]Department of Geology, Faculty of Science, Ferdowsi University of Mashhad, Mashhad, Iran
[3]Department of Geology, Faculty of Earth Science, Shahid Chamran University of Ahvaz, Ahvaz, Iran
[4]Department of Geology, Faculty of Science, University of Zanjan, Zanjan, Iran
[5]Institute of Geosciences, University of Potsdam, Karl-Liebknecht-Strasse 24–25, D-14476 Potsdam, Germany
[6]Laser Lab, Chemistry & Environment Group, Dept. of Analytical Chemistry, University of Zaragoza, 50009 Zaragoza, Spain

(Manuscript received December 2, 2025; accepted in revised form October 15, 2026; Associate Editor: Milan Kohút)

Abstract: The mylonitic granites exposed in the central part of the Sanandaj–Sirjan Zone (CSSZ) are emplaced into the Precambrian basement along the Main Zagros Fault. U–Pb zircon dating of their protolith yields an emplacement age of 297.8±3.9 Ma (Early Permian), consistent with emplacement in a within-plate extensional tectonic setting. The mylonitic granites are classified as transitional A-type, characterised by enrichment of High Field Strength Elements (HFSE) and elevated Nb/Y and Ga/Al ratios. Trace-element systematics, particularly variations in Nb, Hf, Ta, and Zr, indicate a magmatic origin involving significant magma–crust interaction. The $\varepsilon Nd_{(t)}$ values are around 0.9. The isotopic compositions likely reflect post-magmatic disturbance, and the mylonitic granites were later transformed into mylonitic varieties during Mesozoic tectono-thermal reactivation along regional shear zones. Petrographic evidence, including perthitic K-feldspar, well-developed gneissic banding, and advanced dynamic recrystallisation textures, indicates that the Azna mylonitic granites experienced intense dynamic metamorphism. Now, this deformation resulted in partial resetting under lower greenschist-facies conditions within a brittle–ductile regime. Accordingly, the primary crystallisation of the protolith of the Azna mylonitic granite most likely occurred during the late stages of the Variscan orogeny and, within the framework of the proposed model, can be interpreted as being associated with the onset of processes leading to the opening of the Neo-Tethys.

Keywords: Permian mylonitic granite, transitional A-type, U–Pb zircon dating, Rb–Sr isotopes, Sanandaj–Sirjan Zone

Introduction

A-type granites are primarily defined by their geochemical signatures and tectonic affinities and are characterised by elevated SiO_2 and alkali contents, high Fe/Mg ratios, and enrichment in high-field-strength elements such as Zr, Nb, and Y, while typically depleted in Ca, Sr, and Ti (e.g., Eby 1992; Frost et al. 2001; Bonin 2007; Johansson 2023; Breiter 2025; Ondrejka et al. 2025). They commonly originate from high-temperature, anhydrous melts derived from mantle and/or crustal sources and are typically associated with extensional or within-plate tectonic settings (e.g., Collins et al. 1982; Frost & Frost 2011; Qu et al. 2012).

Iran, located within the central segment of the Alpine–Himalayan orogenic belt, records a polycyclic tectono-magmatic evolution shaped by repeated episodes of subduction, continental collision, and post-collisional extension (e.g., Ghasemi & Talbot 2006; Shabanian et al. 2009; Agard et al. 2011). This long-lived geodynamic history encompasses Neoproterozoic to Phanerozoic tectonic events, as documented by numerous studies (Moghadam et al. 2015a; Shabanian et al. 2020; Shakerardakani et al. 2021; Azizi & Whattam 2022).

The CSSZ, forming the inner crystalline core of the Zagros orogen, is widely recognized for its long-lived and diverse magmatic activity from Neoproterozoic to Cenozoic (e.g., Alavi 2004; Esna-Ashari et al. 2012; Shakerardakani et al. 2015; Azizi et al. 2017; Shabanian et al. 2018, 2020). In the Sanandaj–Sirjan Zone (SSZ) of Iran outcrops of A-type granites with various age ranges were reported from other areas by some research works (e.g., Sepahi & Athari 2006; Sepahi 2008; Alirezaei & Hassanzadeh 2012).

The Azna granitoids in the northern SSZ provide an important opportunity to investigate the petrogenesis of A-type magmatism, with the spatially associated Ghaleh-dezh metagranite providing a useful comparison for evaluating the timing, source characteristics, and thermal conditions of Carboniferous granitoid magmatism (Shabanian et al. 2020). This study aims to evaluate U–Pb zircon ages, whole-rock

✉ corresponding author: Ali A. Sepahi
aasepahi@um.ac.ir

Open Access CC BY-NC-ND

geochemical compositions, Sr–Nd isotopic compositions, and electron microprobe (EMPA) data from the Azna granitoids. The dataset is compared with coeval metagranitic bodies from the SSZ and NW Iran to constrain its petrogenesis and tectonic significance, and to re-evaluate the tectonic evolution of the northern Gondwana margin and the previously proposed interpretations for the Ghaleh-dezh granitoids area.

Geological setting

The Zagros Orogen is classically subdivided into three parallel NW–SE trending belts: from southwest to northeast, these are the Zagros Fold-and-Thrust Belt, the SSZ, and the Urumieh–Dokhtar Magmatic Arc (Stöcklin & Nabavi 1973; Fig. 1). It extends for approximately 1500 km along the northeast side of the Main Zagros Fault, with a width varying between 150 and 200 km. The zone is characterized by medium- to high-grade regional metamorphic rocks extensively intruded by igneous bodies ranging from felsic (e.g., Jurassic S-type and A-type granites) to mafic (e.g., gabbro-diorite and basalts) in composition, with magmatic activity concentrated predominantly in the Jurassic (e.g., Hassanzadeh & Wernicke 2016; Azizi & Stern 2019; Nouri et al. 2023).

Neoproterozoic–Cambrian intrusive bodies have high frequency in the SSZ (e.g., Golpaygan, 557 Ma, Moradi et al. 2022; North Shahrekord, 521–513 Ma, Badr et al. 2018; Mahabad, 558–552 Ma, Gholipour et al. 2022; Dorud–Azna mylonitic granites, 608–588 Ma, Shakerardakani et al. 2015) and a suite of Carboniferous–Permian granitoids and mafic intrusions. The latter group comprises the Khalifan granite (ca. 315 Ma, Bea et al. 2011), Ghaleh-dezh metagranite (298–312 Ma, Shabanian et al. 2020), the Hasanrobat granite (ca. 288 Ma, Alirezaei & Hassanzadeh 2012), the Hasansalaran pluton (ca. 360 Ma, Azizi et al. 2017), Dorud–Azna metagabbro (314–336 Ma, Shakerardakani et al. 2015; Fergusson et al. 2016), Gushchi gabbronorite (316–319 Ma, Moghadam et al. 2015b), Gushchi granite (317–318 Ma, Moghadam et al. 2015b; 298–301 Ma, Asadpour et al. 2013b), Moro & Amand granite (350–356 Ma, Mohammadi et al. 2020), Ghazan gabbro (297 Ma, Asadpour et al. 2013a), Sargaz orthogneiss (317–322 Ma, Moghadam et al. 2017), Heris granite (306 Ma, Advay & Ghalamghash 2011), Misho gabbro (356 Ma, Saccani et al. 2013) and the Damamna granite (364–372 Ma, Abdulzahra et al. 2016), Collectively, these Carboniferous–Permian granitoids and mafic intrusions document a widespread episode of late Palaeozoic magmatism across the SSZ (Table 1). Furthermore, several Carboniferous to Permian

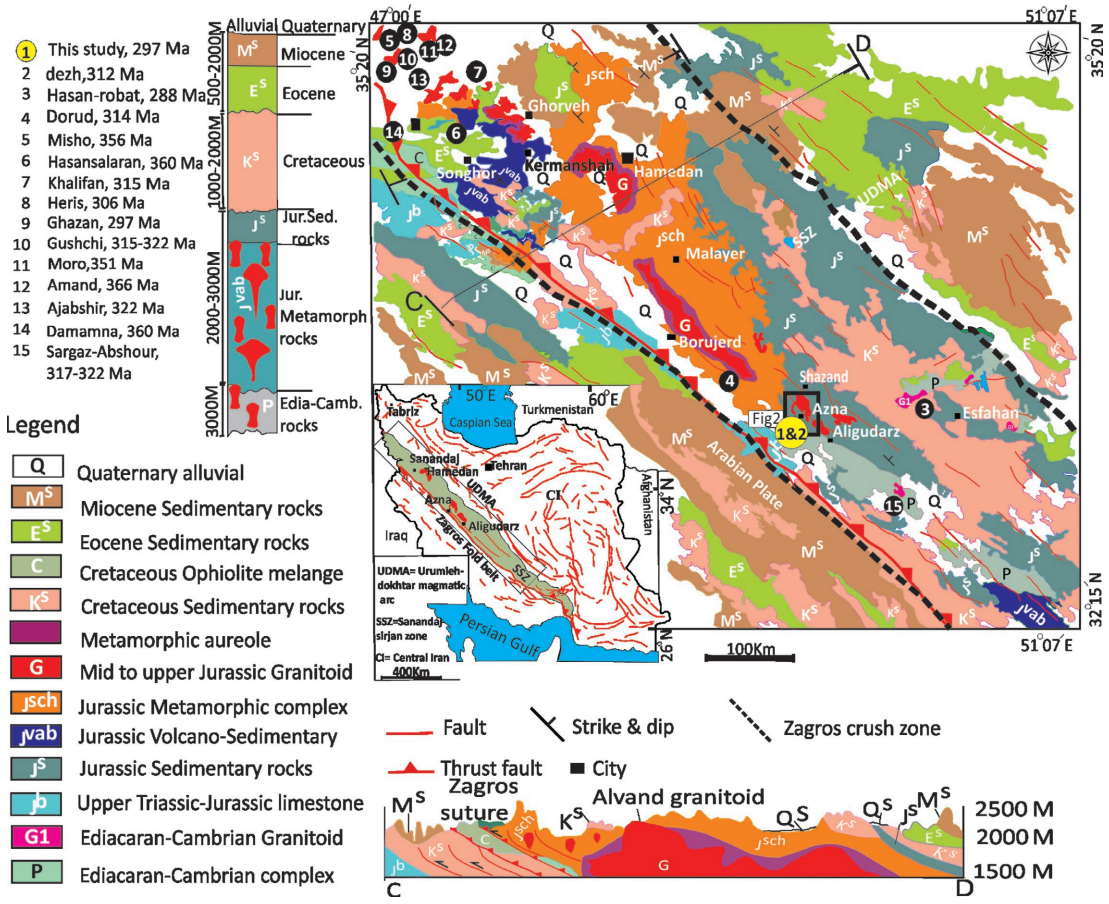


Fig. 1. A schematic geological representation of the SSZ, together with the Zagros fold-thrust system and the Urumieh–Dokhtar magmatic arc (Stöcklin & Nabavi 1973). Futher information is represented in Supplementary Table S1.

Table 1: Summary of previous age data for magmatic rocks from the SSZ zone (Iran) and NE (Iraq).

Area	Rock type	Method	Dated mineral	Magma-type	Geodynamic tectonic	Source	Age (Ma)	Author(s)
North of Sanandaj–Sirjan zone (Iraq)								
Damamna (Iraqi zagros suture zone)	Granite	$^{206}P/^{238}U$	Zircon	A1-type	Extensional intra-continental regime	Enriched mantle with crustal contamination	364.4±8.5, 372.1±3.8	Abdulzahra et al. 2016
North of Sanandaj–Sirjan zone (Iran)								
Misho mafic complex	Gabbro	$^{206}P/^{238}U$	Zircon	A2-type	Initial rift-drift	MORB-type asthenosphere & plum-type material	356.7±3.4	Saccani et al. 2013
Misho complex	Alkali granite, monzogranite, synogranite	Rb/Sr	Whole rock	A2-type	POG	Partial melting of thickened crust	232	Ahankoub et al. 2013
Heris	Granite, alkali granite	$^{207}Pb/^{206}Pb$	Zircon	A2-type	WPG	Lower crust	306±34	Advay & Ghalamghash 2011
Gushchi	Gabbronorite	$^{206}P/^{238}U$	Zircon	A-type		Lower continental crust &/or subcontinental mantle source	319.9±2.5, 316.8±2.3	Moghadam et al. 2015b
Gushchi	Alkali feldspar granite	$^{206}P/^{238}U$	Zircon	A2-type	VAG & WPG	Lower continental crust	318.4±2.3, 317.3±1.9, 322±2.9 298–301	Moghadam et al. 2015b Asadpour et al. 2013b
Moro	Granite	$^{206}P/^{238}U$	Zircon	A-type	WPG		351–356	Mohammadi et al. 2020
Amand	Granite	$^{206}P/^{238}U$	Zircon	A-type	WPG		350.9±1.3	Mohammadi et al. 2020
Ajabshir	Rhyolite	$^{206}P/^{238}U$	Zircon	A-type	WPG		332.5±2.2	Nabatian et al. 2021
Ghazan	Gabbro	$^{206}P/^{238}U$	Zircon	–	WPG		297±6	Asadpour et al. 2013a
Hasansalaran	Granite & monzonite	$^{206}P/^{238}U$	Zircon	A1-type	WPG	Mantle & continental crust	360.2±4.3, 360.7±5.6	Azizi et al. 2017
Khalifan	Leucogranite	$^{206}P/^{238}U$	Zircon	A1- to A2-type		Felsic, infracrustal	315±2	Bea et al. 2011
Sanandaj–Sirjan zone (Iran)								
Hasanrobat	Granite	$^{206}P/^{238}U$	Zircon	A2- to A1-type	WPG	Lower crust (anorogenic intraplate)	288.3±0.6, 294.2±2.5	Alirezaei & Hasanzadeh 2012, Honarmand et al. 2017
Ghaleh dezh	Mylonitic granite	$^{206}P/^{238}U$	Zircon	A2-type	WPG	Mantle–crust	312±12	Shabanian et al. 2020
Meta granite Azna (Ghaleh dezh)	Mylonitic granite	$^{206}P/^{238}U$	Zircon	A-type	WPG	Mantle–crust	297.8±3.9	This study
Dorud	Metagabbro	$^{206}P/^{238}U$	Zircon	–	Back arc rifting	Litospheric or asthenospheric mantle	314.6±3.7 336±9	Shakerardakani et al. 2015, Fergusson et al. 2016
South of Sanandaj–Sirjan zone (Iran)								
Sargaz-Abshour	Orthogneiss	$^{206}P/^{238}U$	Zircon		WPG	–	317–322	Moghadam et al. 2017

magmatic and metamorphic units have been documented in north-western Iran, including amphibolites from the Salmas area (Hajialioghli et al. 2025), Early Carboniferous rhyolites from Ajabshir (Jamei et al. 2021), and Carboniferous–Permian magmatism in the Jolfa region (Delavari et al. 2019). In Central Iran, Permian granitoids (Moghadam et al. 2015b) and Carboniferous–Permian metamorphic rocks of the Anarak complex (Buchs et al. 2013) are interpreted as part of the broader Gondwana related tectonic framework.

The Azna area, located in the central part of the SSZ (Fig. 2), exposes a diverse assemblage of metamorphic and igneous rocks. Metamorphic units include phyllite, schist, marble, and meta-gabbro, which have been affected by amphibolite- to greenschist-facies metamorphism, likely during Jurassic–Cretaceous deformation related to the Zagros orogeny (Alavi 2004; Shabanian et al. 2009, 2020; Agard et al. 2011). The crystalline basement comprises two major components: (i) Upper Neoproterozoic orthogneisses, such as the granitic gneisses of southern Lorestan (Dorud–Azna area; 568±11 Ma, Nutman et al. 2014; 588±41 Ma, Shakerardakani et al. 2015), and (ii) Upper Carboniferous–Lower Permian mylonitic granites exposed locally in the Azna region (Shabanian et al. 2020). Whereas the Precambrian basement fragments form regionally extensive orthogneissic bodies with well-developed gneissic foliation, the mylonitic granites occur as small, localized outcrops characterized by a penetrative mylonitic fabric. The metamorphic rocks are intruded by several igneous bodies, predominantly granites, granodiorites, and quartz diorites of Middle to Late Jurassic age (Esna-Ashari et al. 2012; Shabanian & Neubauer 2024). In the Dorud region, Ediacaran–Cambrian orthogneisses are structurally juxtaposed with the Middle Jurassic Darijune gabbro (170.2±3.1 Ma) (Shakerardakani et al. 2015). The Azna area is dissected by three principal fault systems trending NE–SW, NW–SE, and E–W.

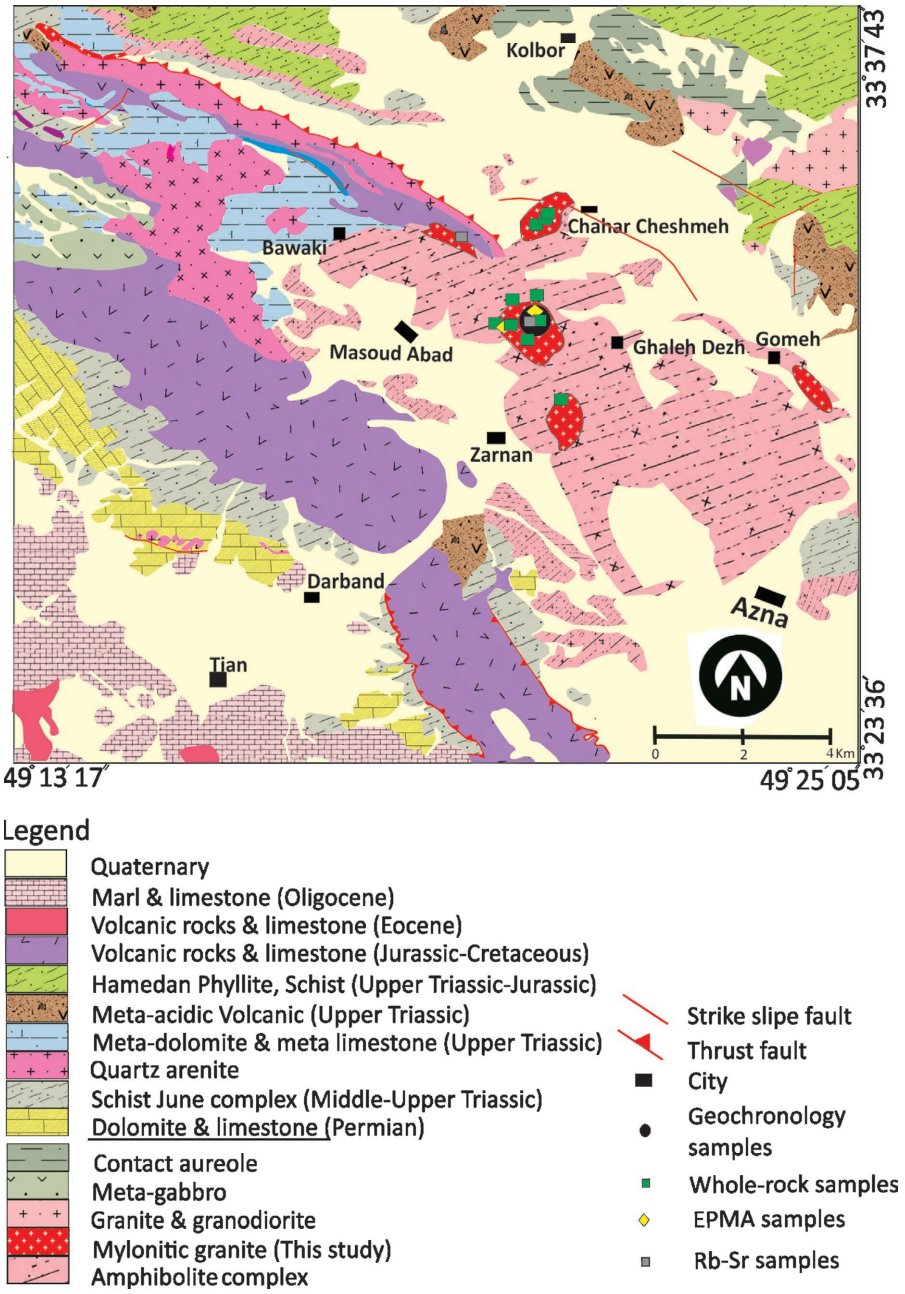


Fig. 2. A generalised geological map of the northern Azna region, compiled by Sahandi et al. (2006) and Shabanian et al (2020).

These fault systems record polyphase deformation involving strike-slip, reverse, and extensional reactivation (Mohajjel & Fergusson 2000; Shakerardakani et al. 2015). Deformation intensifies northward, where Jurassic–Early Cretaceous D2 dextral transpression (~178–170 Ma and ~110 Ma) produced strong mylonitic fabrics and associated kinematic indicators (Moazzen et al. 2004; Babaahmadi et al. 2021). Mylonitic granite bodies display irregular to elongated outcrop patterns controlled by the regional structural fabric and are exposed as discontinuous ridges, with the largest exposures occurring in the Ghaleh-Dezh area (Shabanian et al. 2009, 2020). Their mylonitic foliation is defined by alternating quartz–feldspar-rich and mica-rich bands, augen feldspar porphyroclasts, quartz ribbons, and the preferred orientation of biotite and muscovite, all indicating intense ductile deformation (Fig. 3b).

Petrography

The mylonitic granites are dominated by quartz and feldspars (microcline, orthoclase and plagioclase), along with biotite and muscovite (Fig. 4a–e). Accessory minerals include zircon, titanite, allanite and iron oxides such as magnetite, while chlorite and sericite occur as secondary minerals

(Fig. 4a, f). The rocks exhibit a well-developed mylonitic fabric defined by a fine-grained, dynamically recrystallised aggregate of quartz, muscovite, biotite, and chlorite (Fig. 4d–f). Additional evidence for mylonitisation includes quartz ribbons, feldspar and albite porphyroclasts with undulose extinction and asymmetric pressure shadows, and localized shear bands. Orthoclase, microcline, albite and allanite form the porphyroclasts (Fig. 4a–f). Quartz grains display features consistent with subgrain rotation recrystallisation under shear deformation, forming fine-grained aggregates aligned parallel to the mylonitic foliation. Locally, the foliation is folded, indicating progressive deformation (Hirth & Tullis 1992; Stipp et al. 2002; Passchier & Trouw 2005; Heilbronner & Tullis 2006) (Fig. 4d–f). The lepidogranoblastic texture is clearly visible in Fig. 4b–f. Asymmetric albite porphyroclasts are observed within the mylonitic foliation (Fig. 4d, e).

Analytical methods

LA–ICP–MS analyses

Zircon crystals were separated from a representative mylonitic granite sample selected for U–Pb zircon geochronology using conventional density and magnetic separation techniques at the Laboratory of the Geological Team of Hebei Province, China. Handpicked crystals were mounted on 1-inch epoxy discs with double-sided tape and analysed in random order. U–Pb dating was performed by depth-profiling laser ablation–inductively coupled plasma–mass spectrometry (LA–ICP–MS) following the analytical procedures described by (Liu et al. 2022). Cathodoluminescence (CL) imaging of zircon grains was carried out at Zhongkekuangyan LLC, Beijing, using an electron microprobe to characterize internal zoning and textural features, although these images were not used directly for age determinations. Zircon analysis was undertaken at the Milma LA–ICP–MS facility, China University of Geosciences, Beijing. Laser ablation was conducted with a NewWave 193UC excimer system, coupled to an Agilent 7900 ICP–MS. Analytical conditions included a 35 µm spot size, 10 Hz repetition rate, and an energy density of ~3 J·cm^{-2}. Each analysis consisted of a 20 s background acquisition, 40 s ablation, and 20 s washout. Instrumental mass bias and elemental fractionation were corrected using zircon 91500 as the primary reference material (Wiedenbeck 1995; Wiedenbeck et al. 2004), analysed twice for every ten unknowns. Additional zircon standards GJ-1 (Morel et al. 2008) and Plešovice (Sláma et al. 2008) were interspersed with the unknowns and treated as blind samples to monitor accuracy. The weighted mean $^{206}Pb/^{238}U$ ages obtained were 296.8±2.9 Ma (2σ, n=4) for Plešovice, which is consistent with their recommended values (Jackson et al. 2004; Sláma et al. 2008). Isoplot 4.15 (Ludwig 2012) was employed to generate the geochronological plots. Zircon grains were analysed from two mylonitic granite samples (MG) (Supplementary Table S1).

Electron microprobe analyses

Two fresh and well-preserved mylonitic granite samples were selected for the EMPA. The analyses were performed at the Institute of Geosciences, University of Potsdam (Germany), using a fully automated JEOL JXA-8200 electron microprobe. This instrument, equipped with five wavelength-dispersive spectrometers, was operated at an accelerating voltage of 15 kV, a beam current of 20 nA, and a spot diameter ranging from 2 to 10 µm. Calibration was performed throughout each session using secondary standards to ensure accuracy. The instrument was standardised against natural silicate and oxide reference materials supplied by the Smithsonian Institution and Astimex Standards Ltd., and the built-in ZAF matrix correction procedure was applied to all measurements. Scanning electron microscopy (SEM) and energy-dispersive X-ray spectroscopy (EDXS) analyses were conducted on a JEOL JSM-6510 microscope equipped with a tungsten filament and an Oxford Instruments Xplore30 EDX detector, also housed at the University of Potsdam. In total, 28 albite, 15 K-feldspar, 16 biotite, 8 muscovite, and 14 titanite analytical points were examined by EPMA (Supplementary Tables S2, S3, S4, S5 and S6).



Fig. 3. (a) View of the most prominent mylonitized outcrop in the Azna area. **(b)** Quartz and feldspar porphyroclasts in mylonitic granite are surrounded by mica-rich bands.

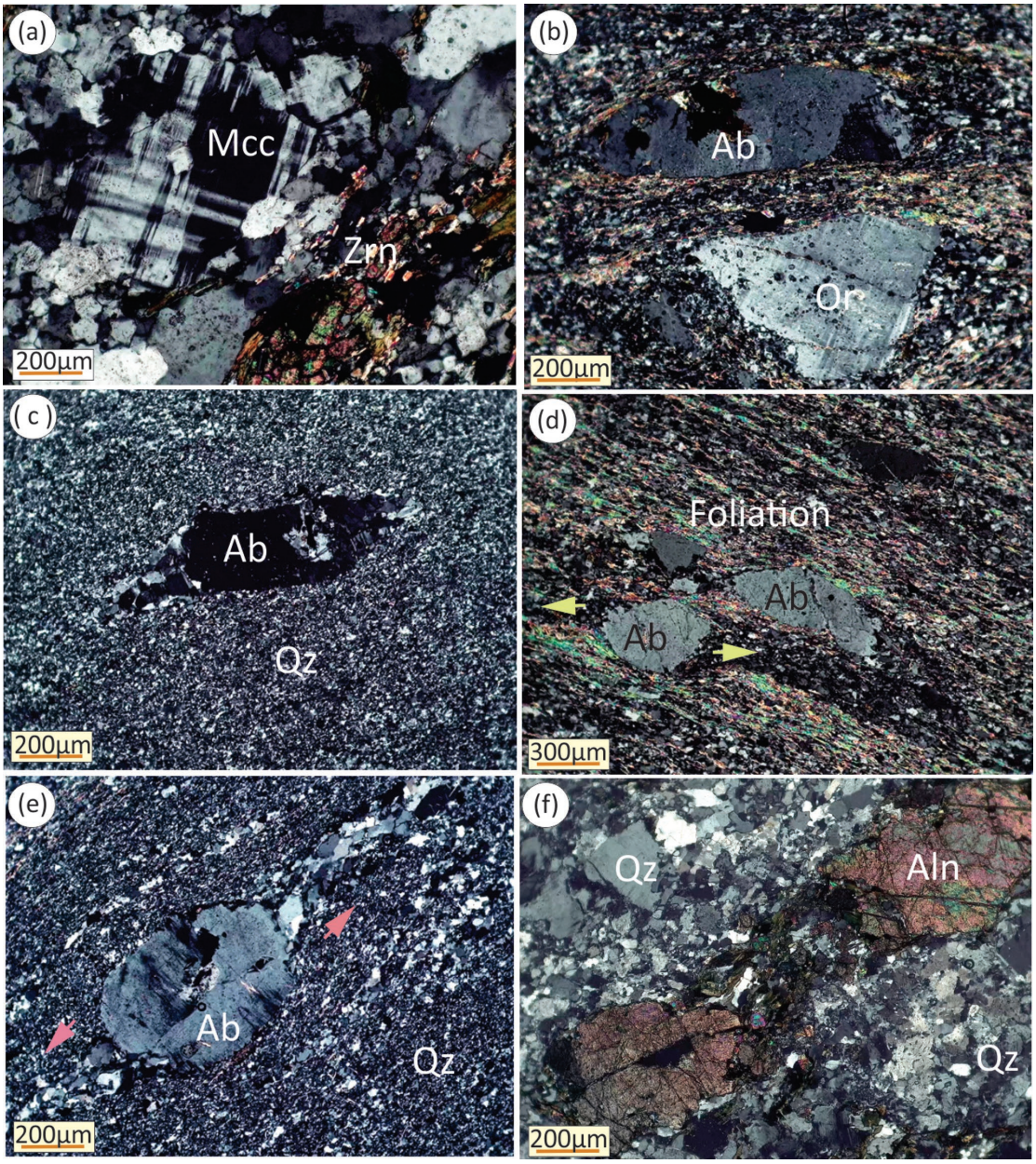


Fig. 4. Photomicrographs of the mylonitic granites from the north of Azna. **(a)** Juxtaposition of microcline porphyroblasts with quartz, XPL. **(b)** Types of albite and polysynthetic twinning in plagioclase minerals, XPL. **(c)** Juxtaposition of albite porphyroblasts with foliations of finer-grained minerals, XPL. **(d)** Scattered albite porphyroclasts with asymmetric mantles, indicated by arrows. **(e)** Albite crystal within a quartz-rich matrix showing a lepidogranoblastic texture. **(f)** Allanite in a matrix of fine-grained quartz and sericitized minerals, XPL. XPL = cross-polarized light; PPL = plane-polarized light. The mineral abbreviations are from Warr (2021).

Whole-rock geochemistry

Ten fresh and unaltered rock samples were selected for whole-rock geochemical analysis. The geochemical analyses were conducted at the Servicio General de Apoyo a la Investigación (SAI) Laboratory, University of Zaragoza, using ICP–MS and XRF techniques. Approximately 0.05 g of powdered sample was digested by microwave-assisted acid digestion in a mixture of 9 mL HNO_3, 3 mL HCl, and 3 mL HF (180 °C for 20 minutes following a 15-minute ramp). The resulting solution was diluted to a final volume of 50.00 mL. ICP-MS analyses were performed using an Agilent 7900 instrument equipped with a crossflow nebulizer, Scott spray chamber, and platinum cones, with rhodium (Rh) as the internal standard. The instrument operated in peak hopping mode at 1.2 kW RF power, with plasma, auxiliary, and nebulizer gas flows of 15, 1.2, and 1.0 L/min, respectively. The ICP-MS precision was better than 3 % RSD. In addition to ICP–MS analyses, three whole-rock samples (Dzh, A1-ab, and Ba-1) were analysed using Laser-Induced Breakdown

Spectroscopy (LIBS) at the University of Zaragoza. The analyses were performed using a Q-switched Nd:YAG laser (Brilliant Quantel, Ultra CFR model) operating at 1064 nm, with an 8 ns pulse duration and a maximum pulse energy of 50 mJ. The laser beam diameter was 2.6 mm. The plasma emission was generated in a LIBS-SC chamber (Ocean Optics) under a controlled Ar atmosphere. The emitted radiation was collected via an optical fibre (QP50-2-UV-BX, Ocean Optics) and transferred to an Echelle spectrometer (Andor Mechelle ME5000; focal length 195 mm, F/7), coupled with an ICCD detector (Andor iStar DH734, 1024×1024 pixels, 13.6×13.6 µm pixel size). The selected analytical conditions included a pulse energy of 25 mJ, a delay time of 725 ns, and an integration gate of 1100 ns (Supplementary Table S7).

Sr–Nd isotopic analysis

Two fresh and unweathered mylonitic granite samples were collected from outcrops in northern Azna for isotopic analysis. Sr–Nd isotopic analyses were conducted at the Radiogenic Isotope Laboratory, METU Central Lab. Analytical procedures followed in-house protocols based on (Köksal 2019). All procedures were performed with ultrapure reagents and Milli-Q water in a class-100 clean lab. About 80 mg of each sample was digested in 4 mL of 52 % HF at >100 °C for four days. Solutions were dried, re-dissolved in 6 N HCl, dried again, and finally dissolved in 2.5 N HCl for cation-exchange chromatography. Strontium was separated using 2 mL of Bio-Rad AG50W-X8 (100–200 mesh) cation resin in Teflon columns and eluted with 2.5 N HCl. Following Sr collection, the rare earth element (REE) fraction was retrieved with 6 N HCl. Sr was loaded on a single Re filament with Ta activator and 0.005 N H_3PO_4 and analysed in static mode. The measured $^{87}Sr/^{86}Sr$ ratios were normalised to $^{86}Sr/^{88}Sr = 0.1194$. The NIST SRM 987 Sr standard yielded an average value of 0.710249 ±5. Neodymium was further separated from the REE fraction using 0.22 N HCl and 2 mL of HDEHP (bis-2-ethylhexyl phosphate)-coated Bio-Rad resin in Teflon columns. The purified Nd was loaded onto double rhenium filaments with 0.005 N H_3PO_4 and measured in static mode. The $^{143}Nd/^{144}Nd$ ratios were normalised to $^{146}Nd/^{144}Nd=0.7219$. The La Jolla Nd standard (Lugmair et al. 1975) produced a value of 0.511848 ± 4. Sr and Nd isotopes were measured on a TRITON TIMS in multi-collection mode without bias correction; uncertainties are reported at 2σ (Supplementary Table S8).

Results

Zircon U–Pb age data

Zircon grains were separated from a mylonitic granitic sample collected from the study area at coordinates 33°31’11”N, 49°21’38”E. Fresh and inclusion-free zircon grains were handpicked for LA–ICP–MS analysis. In total, 73 analytical spots were measured on 50 zircon grains. Most grains exhibit elongate prismatic morphologies and complex internal zoning, including oscillatory and restitic zoning, as well as features indicative of magmatic corrosion (Fig. 5). U/Pb isotopic ratios were measured, and the Th/U ratios and the calculated zircon ages are listed in Supplementary Table S1.

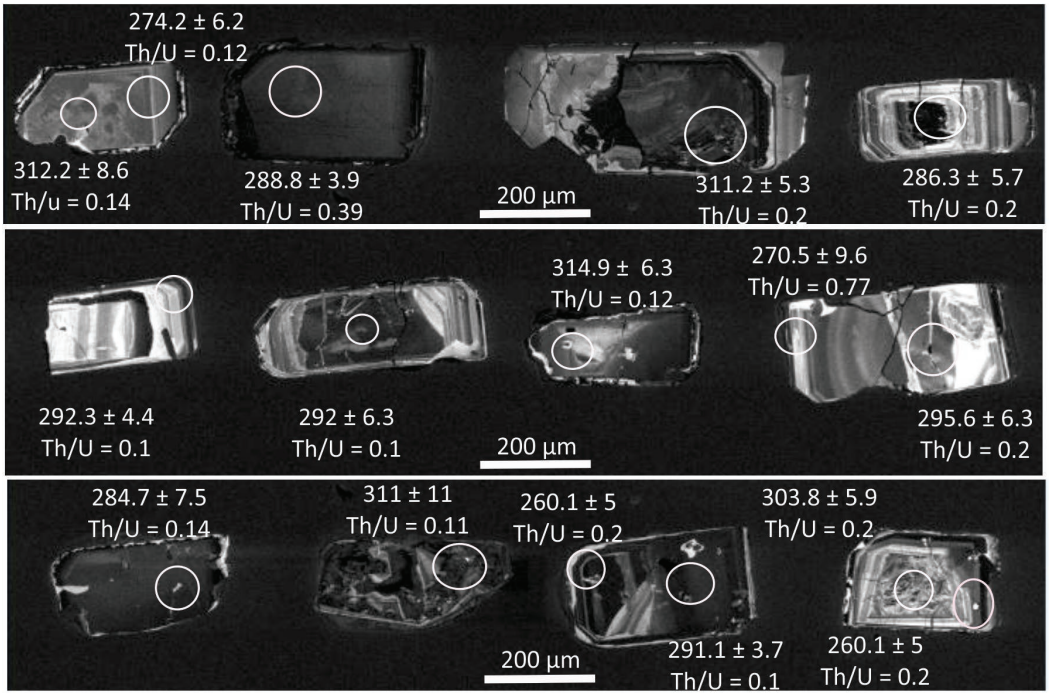


Fig. 5. Selected cathodoluminescence (CL) images of zircon grains extracted from the northern Azna mylonitic granite.

Of the total analytical spots, 17 were discordant. Zircon grains are prismatic crystals exhibiting well-developed oscillatory zoning with some grains exhibiting sector zoning and inherited cores. with bright to dark luminescence in cathodoluminescence images. The zircon grains display lengths between 180 and 300 μm, with length-to-width proportions ranging from 2.25 to 3. The Th/U ratios range from 0.043 to 1.20, with the majority of values exceeding 0.2. For age calculation, only concordant and coeval analyses with <10 % discordance and common Pb content below 2 % were considered. The oscillatory zoning and Th/U ratios of ~0.2 are consistent with magmatic crystallisation (e.g., Rubatto 2002; Hoskin & Schaltegger 2003). The Concordia diagram yields a $^{206}Pb/^{238}U$ age of 297.8±3.9 Ma (MSWD=2.7; 95 % confidence; Fig. 6a), whereas the weighted mean age is 298.4±3.9 Ma (MSWD=2.3; Fig. 6b). The clustered analyses, as shown in the histograms (Fig. 6c), predominantly fall within the 297, 305 and 313 Ma range. The presence of younger discordant ages in the supplementary data table the presence of minor lead loss during subsequent Jurassic magmatic or thermal events.

Mineral chemistry

The plagioclase and K-feldspar chemical compositions are represented in Supplementary Tables S2 and S3. The analysed plagioclase crystals ($Ab_{0.894–0.988} – An_{0.007–0.099} – Or_{0.005–0.011}$) are dominantly albite-rich, whereas K-feldspar grains ($Ab_{0.028–0.052} – An_{0.00–0.020} – Or_{0.948–0.972}$) show compositions close to the orthoclase end-member (Supplementary Fig. S1a). They are in the albite and orthoclase fields on the Ab–Or–An ternary classification. The biotite grains contain 0.539 to 0.66 atoms per formula unit a.p.f.u. Mg, 2.009 to 2.166 a.p.f.u. Fe^{2+} and 3.043–3.920 Fe/Mg ratio in (Supplementary Table S4). The coexistence of secondary and reequilibrated primary biotite reflects a polyphase geological history (Verschure et al. 1980; Nachit et al. 2005) (Supplementary Fig. S1b). The biotite composition plots in the annite field in the siderophyllite–eastonite–annite–phlogopite quadrilateral (Supplementary Fig. S1c). The primary muscovite crystals contain 3.22 a.p.f.u. Si, 2.39 to 2.49 a.p.f.u. Al, and 0.105 to 0.125 a.p.f.u. Mg. Na and Ti range from 0.018 to 0.029 a.p.f.u., and 0.008 to 0.014 a.p.f.u., respectively, in (Supplementary Table S5). Based

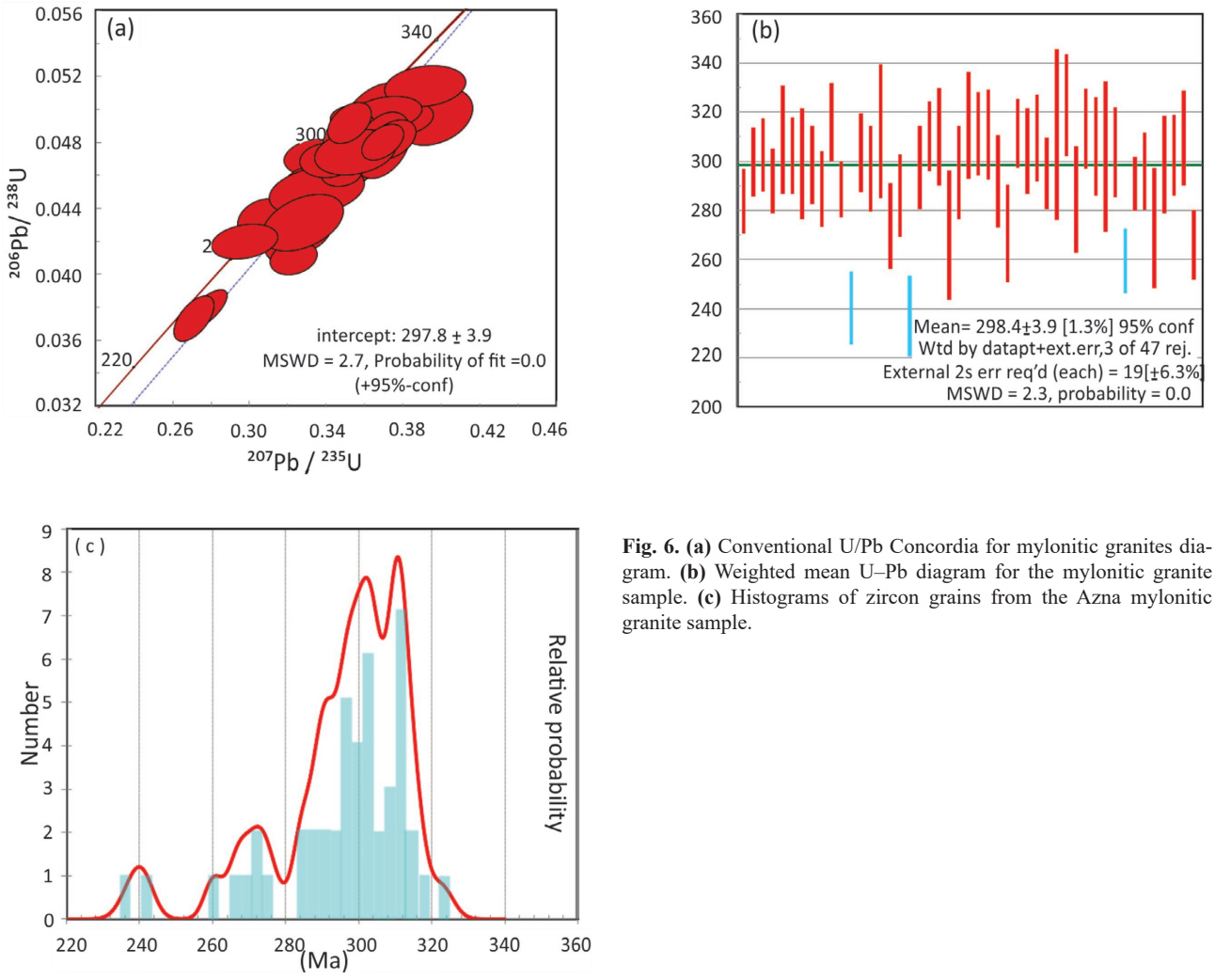


Fig. 6. (a) Conventional U/Pb Concordia for mylonitic granites diagram. **(b)** Weighted mean U–Pb diagram for the mylonitic granite sample. **(c)** Histograms of zircon grains from the Azna mylonitic granite sample.

on their Mg, Na, and Ti contents, they are classified as phengitic muscovite (Supplementary Fig. S1d, e). The titanite grains show variations in Ti (0.610–0.751), Si (0.990–1.078), Al (0.111–0.328), Ca (0.975–1.025) a.p.f.u and Fe^{3+} (0.024–0.080) a.p.f.u. in (Supplementary Table S6). The titanites are interpreted as predominantly magmatic based on their euhedral to subhedral morphology, textural association with primary igneous minerals, relatively uniform composition, and elevated TiO_2 and CaO contents, consistent with the characteristics of magmatic titanite reported by McLeod et al. (2011). The low Ti and Al concentrations reflect low-temperature crystallization (Buddington & Lindsley 1964; Nadoll et al. 2015).

Whole-rock geochemistry

A total of 10 mylonitic granite samples from the Azna area were selected for whole-rock geochemical analysis. To assess regional geochemical trends, these data were compared with published datasets from the Ghaleh-dezh (metagranite Azna; Shabanian et al. 2009, 2020), (Khalifan leucogranite; Bea et al. 2011), (Misho alkaligranite; Ahankoub et al. 2013), (Hasanrobat granite; Alirezaei & Hassanzadeh 2012) and (Hasan salaran granite; Azizi et al. 2017) representing comparable felsic intrusions in the SSZ and adjacent regions. Further information on the comparative datasets is provided in Table 1. The R_1–R_2 diagram (De la Roche et al. 1980), classifies the samples as granites, granodiorite and quartz-syenite (Fig. 7a). The samples contain high SiO_2 (66–77 wt%) and Al_2O_3 (10–15 wt%) and low to moderate Fe_2O_3 (1.2–3.7 wt%) in (Supplementary Table S7). The rocks are peraluminous and belong to the calc-alkaline magma series (Fig. 7b, c).

In the primitive mantle (Sun & McDonough 1989) and upper crust normalised diagrams (Taylor & McLennan 1995) (Fig. 8a, b), the patterns are relatively parallel, showing enrichment in large ion lithophile elements (LILEs), light rare earth elements (LREEs), and high field strength elements (HFSEs) compared to heavy rare earth elements (HREEs). The Azna mylonitic granites (Fig. 8a) are enriched in Rb, Pb, K, and U, but depleted in P. The Khalifan leucogranite (Bea et al. 2011)

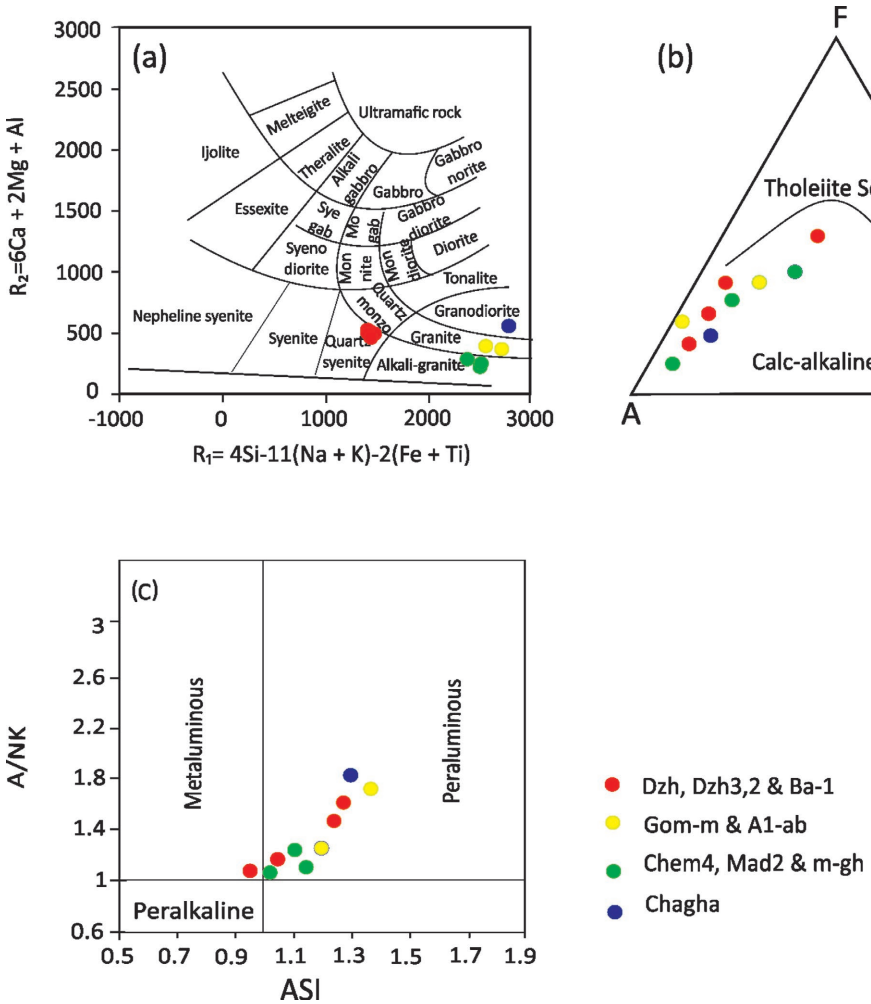


Fig. 7. (a) R_1 vs. R_2 Plot (De la Roche et al. 1980). The plot illustrates that the samples fall within the fields of granite (n=2), granodiorite (n=1), alkali granite (n=3), and quartz syenite (n=4). **(b)** AFM Plot (Irvine & Baragar 1971), all samples are classified as calc-alkaline. **(c)** Diagram for Assessing Magma source (Frost et al. 2001). The samples plot within the peraluminous field.

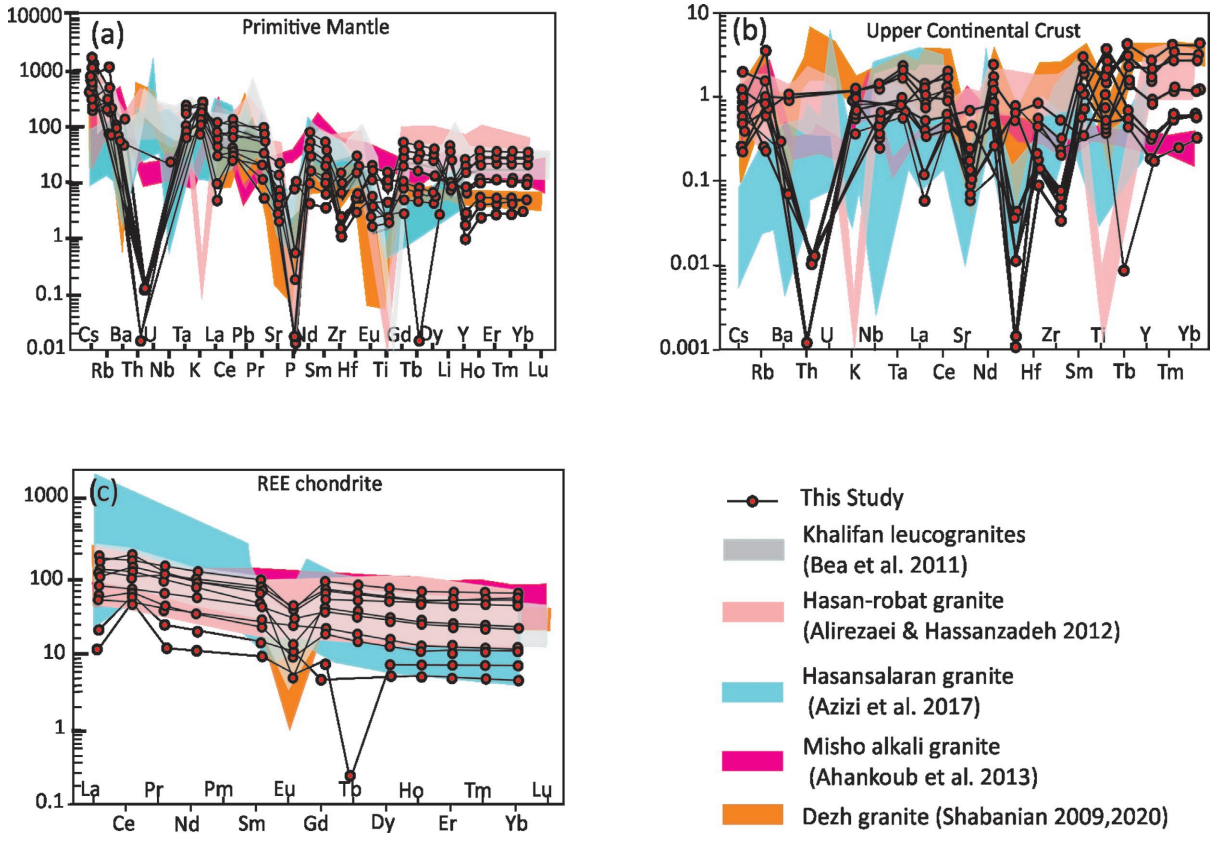


Fig. 8. Trace and REE distribution patterns for the samples were normalised to: **(a)** the primitive mantle (Sun & McDonough 1989); **(b)** upper continental crust (Taylor & McLennan 1995); **(c)** Chondrite (Boynton 1984).

and Hasanrobat granite (Alirezaei & Hassanzadeh 2012) show negative Ti, K anomalies, while the Hasan salaran granite (Azizi et al. 2017) also exhibits depletion in Nb, Ba, and K. The Ghaleh-dezh (Shabanian 2009) rocks are characterized by a stronger negative Eu anomaly and an upward Th and Rb trend relative to the studied samples (Fig. 8a–c). Compared to the upper crustal source (Fig. 8b), the Azna granite mylonite exhibits positive anomalies in high-field strength elements such as Hf, Ti, Zr, Tb, Y, Tm, and Yb. The chondrite-normalised REE patterns (Boynton 1984) (Fig. 8c) of the Azna mylonitic granites show enrichment in light REEs relative to heavy REEs (La_N/Yb_N=2.7–11.8) and display negative Eu anomalies (Eu/Eu*<0.5). The comparative data also exhibit negative Eu anomalies. The LaN/YbN ratios range from 5.8 to 9.4 in the Hasanrobat granites, 7.9 to 18.4 in the Khalifan granites, 2.1 to 54.83 in the Hasan Salaran granites, 8 to 17 in the Misho alkaligranites, and 1.82 to 10.62 in the Ghaleh-dezh granites.

Sr–Nd isotopes

The results of the Sr–Nd isotopic analyses of mylonitic granite samples are summarised in Supplementary Table S8. The samples exhibit relatively high Rb contents, 112, and comparatively lower Sr concentration about 73 ppm. The Rb/Sr value is 1.534. The Nd and Sm contents is 17.27 ppm and 3.43 ppm, respectively. Initial isotopic ratios of Sr and Nd were calculated based on the weighted mean U–Pb zircon age of 297.8 Ma. The initial $^{87}Sr/^{86}Sr_{(i)}$ ratio is 0.7334, while the $^{143}Nd/^{144}Nd$ ratio is approximately 0.5123. The calculated $\varepsilon Nd_{(t)}$ values is about 0.9. Additional information regarding the Sr–Nd isotopic data and the incorporation of data from Shabanian et al. (2020) is provided in the note below Supplementary Table S8.

Discussion

Tectonic setting and petrogenesis

In the tectonic discrimination diagrams (Fig. 9a), most of the Azna mylonitic granite samples and the other compared samples plot within the WPG field, whereas a few samples plot in the volcanic arc to syn-collisional fields, indicating some geochemical variability within the suite. The Azna mylonitic granites show some A-type affinity (Fig. 9b, c), and may have a combined crustal and mantle contributions (Sylvester 1998; Frost & Frost 2011). Geochemically, these rocks are characterized by relatively high concentrations of high field strength elements (HFSEs) such as Zr, Nb, Ce, and

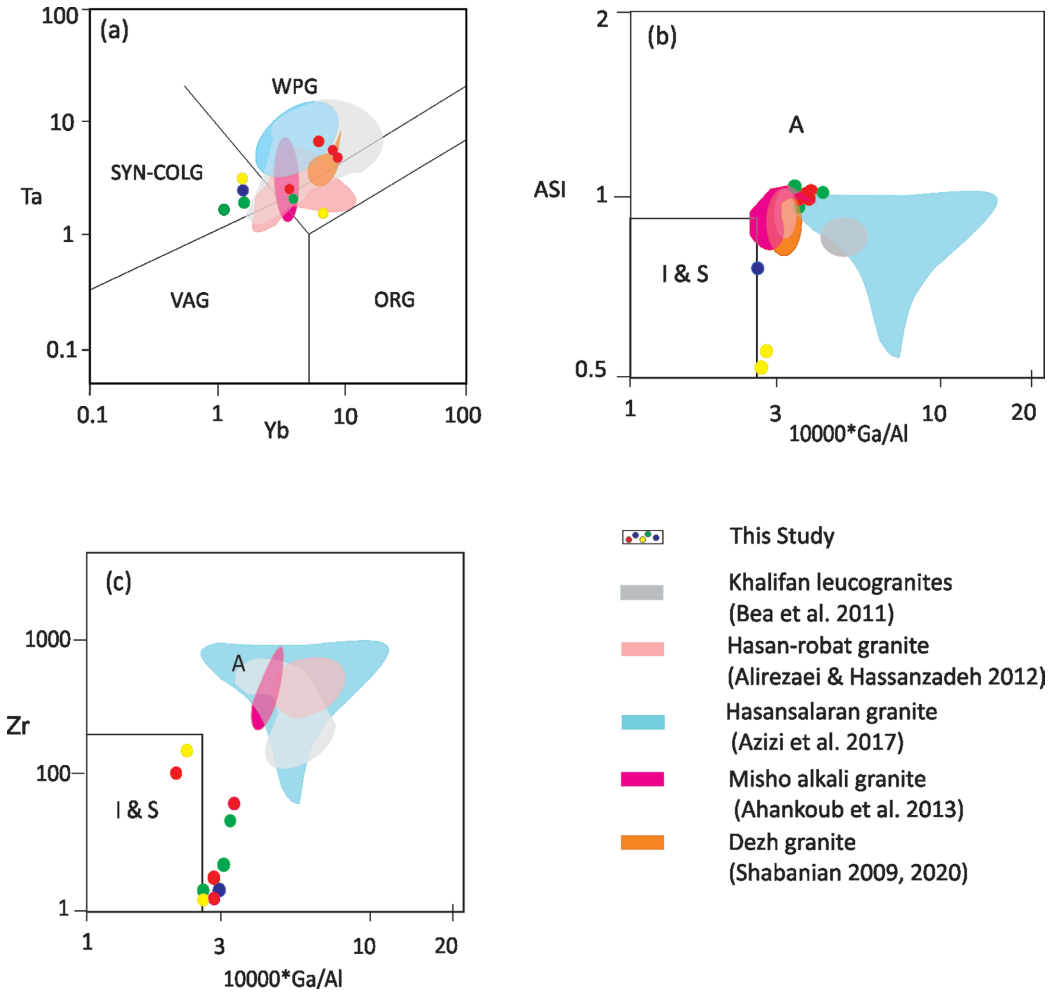


Fig. 9. (a) Tectonic setting discriminating diagrams (Pearce et al. 1984) for the Azna mylonitic granites. **(b, c)** Plots for classifying type granitoids (Whalen et al. 1987).

Y, along with elevated Ga/Al ratios. Trace element ratios, including Th/Yb and Nb/Yb, suggest a significant crustal contribution and limited mantle input. In addition, the enrichment of LREEs relative to HREEs and the pronounced negative Eu anomalies further support extensive partial melting and significant crustal involvement in the petrogenesis of these granites (Pearce et al. 1984). In the Fig. 9b, c and Table 1 this study data (A-Type) and those from Hasan salaran (A1), Khalifan (A1–A2), Hasanrobat, Misho and Ghaleh-dezh (A2) granites presented (Bea et al. 2011; Alirezaei & Hassanzadeh 2012; Ahankoub et al. 2013; Azizi et al. 2017; Shabanian et al. 2020) are presented. High Ga and Nb contents, together with Rb–Ba enrichment and Sr depletion, indicate partial melting of felsic crustal sources (Ji et al. 2022; Wang et al. 2024). The negative Eu anomaly and enrichment in incompatible elements (Rb, Th, Pb, and U) may reflect source characteristics and/or fractional crystallisation, particularly plagioclase fractionation, and may also indicate some contribution from continental crustal materials (Wilson 1989). The mylonitic granites studied in this research show $^{87}Sr/^{86}Sr_{(t)}$ ratio of about 0.7341 and the $^{143}Nd/^{144}Nd_{(t)}$ ratio is approximately 0.5123. This combined isotopic data favour partial melting of an old evolved continental crust and/or assimilation of heterogeneous continental crust with a small contribution from a relatively juvenile mantle-derived component, followed by fractional crystallization during magma evolution. The whole-rock Rb–Sr isochron for the Ghaleh-dezh mylonitic granite yields an age of 274 Ma (Fig. 10a). These samples exhibit ratios ranging from 0.703 to 0.713, suggesting the involvement of both mantle and crustal sources (Fig. 10b) (Ahankoub et al. 2013; Shabanian et al. 2020) reported initial $^{87}Sr/^{86}Sr$ ratios of >0.712 for the Misho granitoids. The $^{87}Sr/^{86}Sr_{(i)}$ ratios vary from 0.649 to 0.711 in the Hasan salaran granites (Azizi et al. 2017) and from 0.738 to 0.834 in the Khalifan granites (Bea et al. 2011), reflecting variable degrees of crustal assimilation and source heterogeneity. The near-chondritic to slightly negative $\varepsilon Nd_{(t)}$ values (+0.2 to −2.8), together with relatively radiogenic initial $^{87}Sr/^{86}Sr$ ratios, indicate a predominantly crustal magma source with a minor mantle contribution.

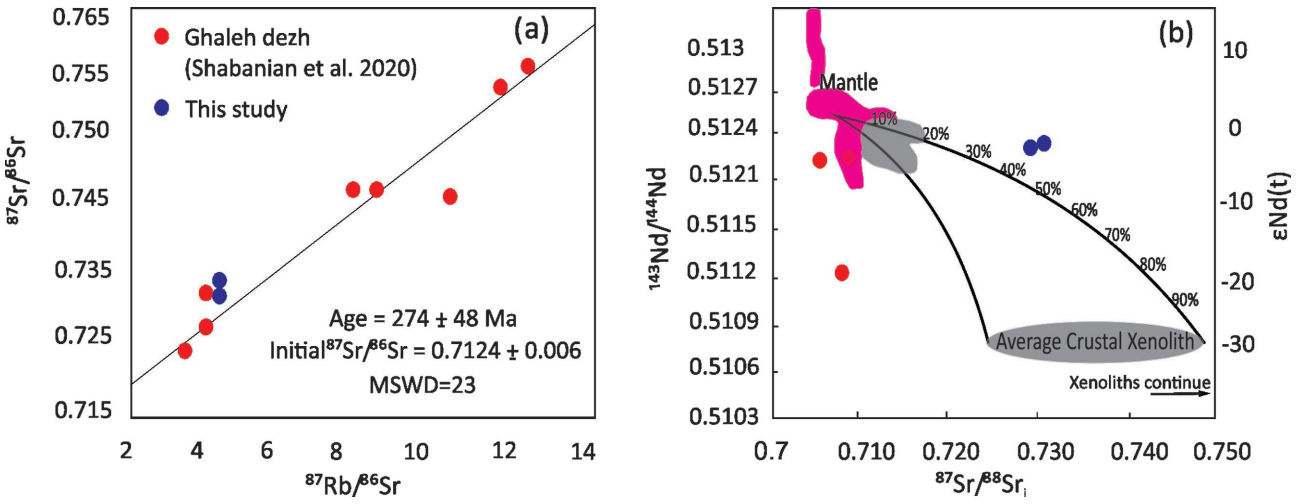


Fig. 10. (a) Whole-rock Rb–Sr isochron of the Ghaleh–Dezh metagranite (274 Ma). **(c)** $^{143}Nd/^{144}Nd$ vs. $^{87}Sr/^{86}Sr_{(i)}$.

Genesis

The majority of zircon grains display Th/U ratios of 0.2 and above, with an average Th/U of 0.26, along with oscillatory zoning, which indicates a magmatic origin for the dated zircon crystals. The Early Permian emplacement age is consistent with a widespread episode of Late Palaeozoic magmatism recognised in the SSZ (Bea et al. 2011; Alirezaei & Hassanzadeh 2012; Fergusson et al. 2016; Hassanzadeh & Wernicke 2016). This timing suggests that the protolith of the mylonitic granite was emplaced during the final stages of the Variscan orogeny and broadly coincided with the initial evolution of the Neo-Tethys (Moghadam et al. 2015b). Whole-rock trace-element ratios, particularly the wide range in Zr/Hf<37 and Nb/Ta (3.73–9.82), indicate heterogeneous source characteristics and variable contributions from crustal and mantle-derived components during magma generation (Wang 2024). In addition, Zr/Hf ratios (11.39–20.05) are consistent with zircon fractionation during magma evolution and support an evolved magmatic system (Lu 2025). Ghaleh-dezh isotopic data ($^{87}Sr/^{86}Sr$ and $^{143}Nd/^{144}Nd$), 0.707–0.7130 and 0.5123 are consistent with a mantle-derived magma that underwent crustal assimilation and fractional crystallization during its evolution (Shabanian et al. 2020). These are consistent with the proposed origins of the A1- and A2-type of granites (Eby 1992). The whole-rock geochemical data further indicate a peraluminous to slightly metaluminous affinity. Although A-type granites are typically derived from relatively low-H_2O magmas, the hydrous minerals in the studied granitoids are interpreted as secondary. Petrographic evidence, including chloritised biotite and fracture-controlled muscovite, indicates late- to post-magmatic alteration rather than primary magmatic crystallisation. The coexistence of titanite and magnetite is compatible with relatively oxidised magmatic conditions but is not, by itself, sufficient to precisely constrain oxygen fugacity (Broska et al. 2007; Erdmann et al. 2019). Textural evidence, including fine-grained recrystallisation of feldspars and the development of secondary muscovite, points to syn- to post-magmatic deformation and retrograde re-equilibration under greenschist facies conditions (Hentschel 2019; Gardner 2021).

Interpretive tectonic model

The available geochronological data reveal that granitoid magmatism in the Azna region occurred during several distinct episodes. The basement of the region is composed of Pan-African orthogneiss units, including the orthogneiss (568 Ma, Nutman et al. 2014; 588 Ma, Shakerardakani et al. 2015), which was followed by the emplacement of Early Cambrian metagranite (525 Ma; Shabanian et al. 2018). The Late Carboniferous magmatism in the region was bimodal, comprising metagranitic and gabbroic rocks, including ca. 336 Ma gabbros (Fergusson et al. 2016; Shakerardakani et al. 2015). This magmatic episode was followed by Early Permian granitoid magmatism, including the granitoid body investigated in the present study. Furthermore, elongated protoliths of middle Jurassic granites and granodiorites, correlated with the Aligudarz granitoids (Esna Ashari et al. 2012), are locally preserved within parts of the Azna area. The temporal distribution of magmatism reveals a long-lived, multi-stage evolution of the Azna crust.

Following the closure of the Proto-Tethys Ocean during the Ediacaran, the northern margin of Gondwana entered a phase of tectonic instability and crustal reorganisation. (Bea et al. 2011; Abdulzahra et al. 2016). This extensional episode resulted in the fragmentation of the Gondwanan margin and the opening of the Neo-Tethys Ocean between the SSZ and the Zagros (Arabian Plate) (Fergusson et al. 2016; Hassanzadeh & Wernicke 2016). Progressive lithospheric thinning and the consequent increase in geothermal gradient provided the necessary thermal conditions for widespread crustal anatexis

and extensive magmatic activity along the future Zagros suture zone (Hassanzadeh & Wernicke 2016).

U–Pb zircon ages from the Azna granite mylonite and the Ghaleh-dezh metagranite (312–298 Ma) constrain the emplacement and crystallisation of their granitoid protoliths to the waning stages of Syn-Variscan magmatism. The calculated zircon saturation temperatures (T^{Zr}.sat.) of the studied mylonitic granites range from 627 to 846 °C, broadly overlapping with the relatively high T^{Zr}.sat. values reported for the Ghaleh-dezh metagranite (767–879 °C; average 827 °C) by Shabanian et al. (2020). Given the close spatial association between the studied mylonitic granites and the Ghaleh-dezh metagranite, these comparable temperature estimates are consistent with relatively high-temperature conditions during the generation and crystallisation of their granitoid protoliths. During the Early Permian, the northern Gondwanan margin experienced a complex tectonic regime characterised by the coexistence of extensional and compressional processes in different sectors of the margin (Ghasemi & Talbot 2006).

The extensional nature of the Permian event proposed by Mossakovsky (1970) and Belov et al. (1986) does not fully account for the entire geological history and evolution of the Azna granite mylonite along the northern margin of Gondwana. After the final stages of Variscan-related convergence at the northern Gondwanan margin, post-collisional lithospheric relaxation and crustal extension promoted asthenospheric upwelling beneath the Iranian microcontinents. The associated thermal perturbation triggered partial melting of a compositionally heterogeneous lower crust, which had been previously enriched and modified by mantle-derived magmatic contributions (Alirezaei & Hassanzadeh 2012; Hassanzadeh & Wernicke 2016; Shabanian et al. 2020; Ashrafi et al. 2023).

Consequently, widespread felsic magmatism was generated, resulting in the emplacement of the Azna granite mylonite (Ghaleh-dezh) assemblage. The enrichment of these rocks in high field strength elements (HFSE), coupled with negative Eu anomalies and their isotopic characteristics (Shabanian et al. 2020), suggests a hybrid magma source involving variable contributions from both mantle-derived melts and crustal components. Accordingly, the Azna granite mylonite is considered to represent a terminal pulse of Variscan magmatic activity in the SSZ, emplaced during the extensional collapse of the previously thickened northern Gondwanan crust and immediately preceding the initiation of Neo-Tethys rifting. The Azna mylonitic granite generally supports the tectonic framework proposed by (Shabanian et al. 2020) for Late Carboniferous–Early Permian magmatism in the SSZ.

The granite was emplaced at ca. 297 Ma during the late stages of Variscan orogeny and was subsequently modified by tectonothermal events related to the opening and closure of the Neo-Tethys Ocean. Therefore, the Azna mylonite granite records a transition from a predominantly mantle-controlled magmatic system to one in which mantle–crust interaction became the principal mechanism governing magma evolution.

Conclusion

The emplacement age of 297.8±3.9 Ma places the Azna mylonitic granite in the Asselian–early Permian magmatic episode within the SSZ, predating the Jurassic magmatism of the Azna–Aligudarz belt by nearly 130 Myr. The clustered age populations indicate a probable older ca. 313 Ma magmatic event that was subsequently overgrown by the principal magmatic event at ca. 298 Ma. Its near-chondritic $\varepsilon Nd_{(t)}$ value and initial Sr isotopic composition, indicates magma generation through reworking of continental crust with a subordinate mantle contribution. Integrated geochronological, geochemical, and isotopic evidence therefore supports emplacement during the waning stages of the Variscan tectono-magmatic evolution, broadly coeval with the initial development of the Neo-Tethyan realm.

Acknowledgments: We would like to express our sincere gratitude to Professor Franz Neubauer and three anonymous reviewers for constructive reviews, and to Dr. Milan Kohút and Dr. Silvia Antolíková for editorial handling and recommendations to the original manuscript. We have learned a great deal from their valuable guidance and constructive comments, which have greatly improved the quality of our manuscript. We would also like to express our sincere appreciation to our esteemed colleagues, Dr. Li Liu, Dr. Fatma Toksoy-Köksal, and Dr. Serhat Köksal, for their valuable assistance with the geochronological and Rb–Sr isotopic analyses. We express our appreciation to the Laser Lab and acknowledge the support and facilities provided by the Servicio General de Apoyo a la Investigación (SAI) at the University of Zaragoza. Financial support from the Government of Aragon (E49_20 R), the European Social Fund, and the University of Zaragoza is gratefully acknowledged.

References

Abdel-Rahman A.-F.M. 1994: Nature of biotites from alkaline, calc-alkaline, and peraluminous magmas. *Journal of Petrology* 35, 525–541. https://doi.org/10.1093/petrology/35.2.525

Abdulzahra I.K., Hadi A., Asahara Y., Azizi H. & Yamamoto K. 2016: Zircon U–Pb ages and geochemistry of Devonian A-type granites in the Iraqi Zagros Suture Zone (Damamna area): New evidence for magmatic activity related to the Hercynian orogeny. *Lithos* 264, 360–374. https://doi.org/10.1016/j.lithos.2016.09.006

Advay M. & Ghalamghash J. 2011: Petrogenesis and zircon U–Pb radiometric dating in Herris granite (NW Shabestar) East Azarbaijan Province. *Iranian Journal of Crystallography and Mineralogy* 18, 633–646.

Agard P., Omrani J., Jolivet L., Whitechurch H., Vrielynck B., Spakman W., Monié P., Meyer B. & Wortel R. 2011: Zagros orogeny: a subduction-dominated process. *Geological Magazine* 148, 692–725. https://doi.org/10.1017/S001675681100046X

Ahankoub M., Jahangiri A., Asahara Y. & Moayyed M. 2013: Petrochemical and Sr–Nd isotope investigations of A-type granites in the east of Misho, NW Iran. *Arabian Journal of Geosciences* 6, 4833–4849. https://doi.org/10.1007/s12517-012-0680-9

Alavi M. 2004: Regional stratigraphy of the Zagros fold-thrust belt of Iran and its proforeland evolution. *American Journal of Science* 304, 1–20.

Alirezaei S. & Hassanzadeh J. 2012: Geochemistry and zircon geochronology of the Permian A-type Hasanrobat granite, Sanandaj–Sirjan belt: A new record of the Gondwana break-up in Iran. *Lithos* 151, 122–134. https://doi.org/https://doi.org/10.1016/j.lithos.2011.11.015

Asadpour M., Pourmoafi S. M. & Heuss S. 2013a: Geochemistry, petrology and U–Pb geochronology of Ghazan mafic-ultramafic intrusion, NW Iran. *Petrological Journal* 4, 1–16.

Asadpour M., Heuss S. & Pourmoafi S.M. 2013b: New Evidences of Precambrian and Paleozoic Magmatism in the Gharebagh Intrusives, NW Iran. *Scientific Quarterly Journal of Geosciences* 23, 129–148.

Ashrafi N., Pourmohsen M. & Faridazad M. 2023: Study of A-type granite from the South of Lake Urmia, Sanandaj-Sirjan Zone: implications for the Neotethys opening in Iran. *Iranian Journal of Earth Sciences* 15. https://doi.org/10.30495/ijes.2022.1941506.1657

Azizi H. & Stern R.J. 2019: Jurassic igneous rocks of the central Sanandaj–Sirjan zone (Iran) mark a propagating continental rift, not a magmatic arc. *Terra Nova* 31, 415–423. https://doi.org/10.1111/ter.12404

Azizi H. & Whattam S.A. 2022: Does neoproterozoic-early paleozoic (570–530 Ma) basement of Iran belong to the cadomian orogeny? *Precambrian Research* 368, 106474. https://doi.org/10.1016/j.precamres.2021.106474

Azizi H., Kazemi T. & Asahara Y. 2017: A-type granitoid in Hasansalaran complex, northwestern Iran: Evidence for extensional tectonic regime in northern Gondwana in the Late Paleozoic. *Journal of Geodynamics* 108, 56–72. https://doi.org/10.1016/j.jog.2017.05.003

Babaahmadi A., Davoudian A.R. & Mohammad Mohajjel M. 2021: Transpression in the Sanandaj-Sirjan Zone (Zagros Orogen, Iran) during the Jurassic and Early Cretaceous: Evidence from the North Shahrekord Shear Zone. *Journal of Structural Geology* 149, 104387. https://doi.org/10.1016/j.jsg.2021.104387

Badr A., Davoudian A.R., Shabanian N., Azizi H., Asahara Y., Neubauer F., Dong Y. & Yamamoto K. 2018: A-and I-type metagranites from the North Shahrekord Metamorphic Complex, Iran: Evidence for Early Paleozoic post-collisional magmatism. *Lithos* 300, 86–104. https://doi.org/10.1016/j.lithos.2017.12.008

Bea F., Mazhari A., Montero P., Amini S. & Ghalamghash J. 2011: Zircon dating, Sr and Nd isotopes, and element geochemistry of the Khalifan pluton, NW Iran: Evidence for Variscan magmatism in a supposedly Cimmerian superterrane. *Journal of Asian Earth Sciences* 40, 172–179. https://doi.org/https://doi.org/10.1016/j.jseaes.2010.08.005

Belov A., Gatinsky Y.G. & Mossakovsky A. 1986: A precis on pre-Alpine tectonic history of Tethyan paleooceans. *Tectonophysics* 127, 197–211. https://doi.org/10.1016/0040-1951(86)90061-2

Bonin B. 2007: A-type granites and related rocks: evolution of a concept, problems and prospects. *Lithos* 97, 1–29. https://doi.org/10.1016/j.lithos.2006.12.007

Boynton W.V. 1984: Cosmochemistry of the rare earth elements: meteorite studies. *Developments in geochemistry* 2, 63–114. https://doi.org/10.1016/B978-0-444-42148-7.50008-3

Breiter K. 2025: Chemical compositions of zircon from rare-metal granites of different geochemical affiliations – a review. *Geologica Carpathica* 76, 227–243. https://doi.org/10.31577/GeolCarp.2025.15

Broska I., Harlov D., Tropper P. & Siman P. 2007: Formation of magmatic titanite and titanite–ilmenite phase relations during granite alteration in the Tribeč Mountains, Western Carpathians, Slovakia. *Lithos* 95, 58–71. https://doi.org/10.1016/j.lithos.2006.07.012

Buchs D.M., Bagheri S., Martin L., Hermann J. & Arculus R. 2013: Paleozoic to Triassic ocean opening and closure preserved in Central Iran: constraints from the geochemistry of meta-igneous rocks of the Anarak area. *Lithos* 172, 267–287. https://doi.org/10.1016/j.lithos.2013.02.009

Buddington A.F. & Lindsley D.H. 1964: Iron-titanium oxide minerals and synthetic equivalents. *Journal of Petrology* 5, 310–357.

Collins W.J., Beams S.D., White A. & Chappell B. 1982: Nature and origin of A-type granites with particular reference to southeastern Australia. *Contributions to Mineralogy and Petrology* 80, 189–200. https://doi.org/10.1007/BF00374895

De la Roche H., Leterrier J., Grandclaude P. & Marchal M. 1980: A classification of volcanic and plutonic rocks using R1R2-diagram and major-element analyses – its relationships with current nomenclature. *Chemical Geology* 29, 183–210. https://doi.org/10.1016/0009-2541(80)90020-0

Delavari M., Arab Asadi F. & Mohammadi A. 2019: Paleozoic magmatism in the southwest of Julfa (northwestern Iran): geochemical characteristics, U–Pb dating and tectonic setting. *Petrological Journal* 10, 99–120.

Eby G.N. 1992: Chemical subdivision of the A-type granitoids: petrogenetic and tectonic implications. *Geology* 20, 641–644.

Erdmann S., Wang R., Huang F., Scaillet B., Zhao K., Liu H., Chen Y. & Faure M. 2019: Titanite: A potential solidus barometer for granitic magma systems. *Comptes Rendus, Géoscience* 351, 551–561. https://doi.org/10.1016/j.crte.2019.09.002

Esna-Ashari A., Tiepolo M., Valizadeh M.-V., Hassanzadeh J. & Sepahi A.-A. 2012: Geochemistry and zircon U–Pb geochronology of Aligoodarz granitoid complex, Sanandaj-Sirjan zone, Iran. *Journal of Asian Earth Sciences* 43, 11–22. https://doi.org/10.1016/j.jseaes.2011.09.001

Fergusson C.L., Nutman A.P., Mohajjel M. & Bennett V.C. 2016: The Sanandaj–Sirjan Zone in the Neo-Tethyan suture, western Iran: Zircon U–Pb evidence of late Palaeozoic rifting of northern Gondwana and mid-Jurassic orogenesis. *Gondwana Research* 40, 43–57. https://doi.org/10.1016/j.gr.2016.08.006

Frost B.R., Barnes C.G., Collins W.J., Arculus R.J., Ellis D.J. & Frost C.D. 2001: A geochemical classification for granitic rocks. *Journal of Petrology* 42, 2033–2048. https://doi.org/10.1093/petrology/42.11.2033

Frost C.D. & Frost B.R. 2011: On ferroan (A-type) granitoids: their compositional variability and modes of origin. *Journal of Petrology* 52, 39–53. https://doi.org/10.1093/petrology/egq070

Gardner J., Wheeler J. & Mariani E. 2021: Interactions between deformation and dissolution-precipitation reactions in plagioclase feldspar at greenschist facies. *Lithos* 396, 106241. https://doi.org/10.1016/j.lithos.2021.106241

Ghasemi A. & Talbot C.J. 2006: A new tectonic scenario for the Sanandaj–Sirjan Zone (Iran). *Journal of Asian Earth Sciences* 26, 683–693. https://doi.org/10.1016/j.jseaes.2005.01.003

Gholipour S., Azizi H., Masoudi F., Asahara Y. & Minami M. 2022: S-type like granites and felsic volcanic rocks in the Mahabad area, NW Iran: Late Neoproterozoic extensional tectonics follow collision on the northern boundary of Gondwana. *Lithos* 416, 106658. https://doi.org/10.1016/j.lithos.2022.106658

Hajialioghli R., Moazzen M., Saeidi S., Mohammadi A. & Laurent O. 2025: Late Carboniferous–Early Permian geodynamic evolution of NW Iran: Zircon U–Pb ages, Hf isotopes, and whole rock geochemistry of Salmas amphibolites. *Journal of Geodynamics* 164, 102089. https://doi.org/10.1016/j.jog.2025.102089

Hassanzadeh J. & Wernicke B.P. 2016: The Neotethyan Sanandaj-Sirjan zone of Iran as an archetype for passive margin-arc transitions. *Tectonics* 35, 586–621. https://doi.org/10.1002/2015TC003926

Heilbronner R. & Tullis J. 2006: Evolution of c axis pole figures and grain size during dynamic recrystallisation: Results from experimentally sheared quartzite. *Journal of Geophysical Research: Solid Earth* 111, B10. https://doi.org/10.1029/2005JB004194

Hentschel F., Trepmann C.A. & Janots E. 2019: Deformation of feldspar at greenschist facies conditions–the record of mylonitic pegmatites from the Pfunderer Mountains, Eastern Alps. *Solid Earth* 10, 95–116. https://doi.org/10.5194/se-10-95-2019

Hirth G. & Tullis J.A.N. 1992: Dislocation creep regimes in quartz aggregates. *Journal of Structural Geology* 14, 145–159.

Honarmand M., Li X.H., Nabatian G. & Neubauer F. 2017: In-situ zircon U–Pb age and Hf–O isotopic constraints on the origin of the Hasan-Robat A-type granite from Sanandaj–Sirjan zone, Iran: implications for reworking of Cadomian arc igneous rocks. *Mineralogy and Petrology* 111, 659–675. https://doi.org/10.1007/s00710-016-0490-y

Hoskin P.W. & Schaltegger U. 2003: The composition of zircon and igneous and metamorphic petrogenesis. *Reviews in Mineralogy and Geochemistry* 53, 27–62. https://doi.org/10.2113/0530027

Irvine T.N. & Baragar W. 1971: A guide to the chemical classification of the common volcanic rocks. *Canadian Journal of Earth Sciences 8*, 523–548. https://doi.org/10.1139/e71-055

Jackson S.E., Pearson N.J., Griffin W.L. & Belousova E.A. 2004: The application of laser ablation-inductively coupled plasma-mass spectrometry to in situ U–Pb zircon geochronology. *Chemical Geology* 211, 47–69. https://doi.org/10.1016/j.chemgeo.2004.06.017

Jamei S., Ghorbani M., Williams I.S. & Moayyed M. 2021: Tethyan oceans reconstructions with emphasis on the Early Carboniferous Pir-Eshagh A-type rhyolite and the Late Palaeozoic magmatism in Iran. *International Geology Review* 63, 1389–1405. https://doi.org/10.1080/00206814.2020.1768443

Ji M., Gao X.-Y. & Zheng Y.-F. 2022: Geochemical evidence for partial melting of progressively varied crustal sources for leucogranites during the Oligocene–Miocene in the Himalayan orogen. *Chemical Geology* 589, 120674. https://doi.org/10.1016/j.chemgeo.2021.120674

Jiang Y.-H. & Zhu S.-Q. 2017: Petrogenesis of the Late Jurassic peraluminous biotite granites and muscovite-bearing granites in SE China: geochronological, elemental and Sr–Nd–O–Hf isotopic constraints. *Contributions to Mineralogy and Petrology* 172, 101. https://doi.org/10.1007/s00410-017-1422-5

Johansson Å. 2023: A tentative model for the origin of A-type granitoids. *Minerals* 13, 236. https://doi.org/10.1007/s00410-017-1422-5

Köksal S. 2019: The Upper Cretaceous intrusive rocks with extensive crustal contribution in Hacimahmutusagi Area (Aksaray/Turkey). *Geologica Carpathica* 70, 261–276. https://doi.org/10.2478/geoca-2019-0015

Liu L., Zhu D.C., Wang Q., Cawood P.A., Stockli D.F., Stockli L.D., Lin C., Zhang J.J., Zhang L.L. & Zhao Z.D. 2022: Leucogranite records multiple collisional orogenies. *Geophysical Research Letters*49,e2021GL096817.https://doi.org/10.1029/2021GL096817

Lu W., Zhang Z., Yuan J., Zhang Y., Li Q., An Y. & Zhan D. 2025: Petrogenesis of Himalayan Leucogranites: A Perspective from Zircon Trace Elements. *Minerals* 15, 1306. https://doi.org/10.3390/min15121306

Ludwig K.R. 2012: User's manual for Isoplot 3.75: A geochronological toolkit for Microsoft Excel. *Berkeley Geochronology Center Special Publication* 5, 75.

Lugmair G., Scheinin N. & Marti K. 1975: Sm–Nd age of Apollo 17 basalt 75075: two-stage igneous processes in mare basalt genesis. *Abstracts of the Lunar and Planetary Science Conference* 6, 531.

McLeod G.W., Dempster T.J. & Faithfull J.W. 2011: Deciphering magma-mixing processes using zoned titanite from the Ross of Mull Granite, Scotland. *Journal of Petrology* 52, 55–82. https://doi.org/10.1093/petrology/egq071

Moghadam H.S., Khademi M., Hu Z., Stern R.J., Santos J.F. & Wu Y. 2015a: Cadomian (Ediacaran–Cambrian) arc magmatism in the ChahJam–Biarjmand metamorphic complex (Iran): Magmatism along the northern active margin of Gondwana. *Gondwana Research* 27, 439–452. https://doi.org/10.1016/j.gr.2013.10.014

Moghadam H.S., Li X.-H., Ling X.-X., Stern R.J., Santos J.F., Meinhold G., Ghorbani G. & Shahabi S. 2015b: Petrogenesis and tectonic implications of Late Carboniferous A-type granites and gabbronorites in NW Iran: Geochronological and geochemical constraints. *Lithos* 212, 266–279. https://doi.org/10.1016/j.lithos.2014.11.009

Moghadam H.S., Brocker M., Griffin W.L., Li X. H., Chen R.X. & O'Reilly S.Y. 2017: Subduction, high-P metamorphism, and collision fingerprints in South Iran: Constraints from zircon U–Pb and mica Rb–Sr geochronology. *Geochemistry, Geophysics, Geosystems* 18, 306–332. https://doi.org/10.1002/2016GC006585

Moazzen M., Moayyed M., Modjarrad M. & Darvishi E. 2004: Azna granitoid as an example of syn-collision S-type granitisation in Sanandaj-Sirjan metamorphic belt, Iran. *Neues Jahrbuch für Mineralogie – Monatshefte* 11, 489–507. https://doi.org/10.1127/0028-3649/2004/2004-0489

Mohajjel M. & Fergusson C.L. 2000: Dextral transpression in Late Cretaceous continental collision, Sanandaj–Sirjan zone, western Iran. *Journal of Structural Geology* 22, 1125–1139. https://doi.org/10.1016/S0191-8141(00)00023-7

Mohammadi A., Moazzen M., Lechmann A. & Laurent O. 2020: Zircon U–Pb geochronology and geochemistry of Late Devonian–Carboniferous granitoids in NW Iran: implications for the opening of Paleo-Tethys. *International Geology Review* 62, 1931–1948. https://doi.org/10.1080/00206814.2019.1675540

Moradi A., Shabanian N., Davoudian A.R., Azizi H., Santos J.F. & Asahara Y. 2022: Geochronology and petrogenesis of the Late Neoproterozoic granitic gneisses of Golpayegan metamorphic complex: a new respect for Cadomian crust in the Sanandaj-Sirjan zone, Iran. *International Geology Review* 64, 1450–1473. https://doi.org/10.1080/00206814.2020.1821251

Morel M.L.A., Nebel O., Nebel-Jacobsen Y.J., Miller J.S. & Vroon P.Z. 2008: Hafnium isotope characterization of the GJ-1 zircon reference material by solution and laser-ablation MC-ICPMS. *Chemical Geology* 255, 231–235. https://doi.org/10.1016/j.chemgeo.2008.06.040

Mossakovsky A.A. 1970: On the upper Paleozoic volcanic belt of Europe and Asia. *Geotectonica* 4, 65–77.

Nabatian G., Li X.-H., Honarmand M. & Esmaeili R. 2021: The magmatic evolution of the Neotethyan rift: Geochronologic, isotopic, and geochemical evidence from A-type felsic magmatism, NW Iran. *Journal of Geodynamics* 145, 101829. https://doi.org/10.1016/j.jog.2021.101829

Nachit H., Ibhi A. & Ohoud M.B. 2005: Discrimination between primary magmatic biotites, reequilibrated biotites and neoformed biotites. *Comptes Rendus, Géoscience* 337, 1415–1420. https://doi.org/10.1016/j.crte.2005.09.002

Nadoll P., Mauk J.L., Leveille R.A. & Koenig A.E. 2015: Geochemistry of magnetite from porphyry Cu and skarn deposits in the southwestern United States. *Mineralium Deposita* 50, 493–515. https://doi.org/10.1007/s00126-014-0539-y

Nouri F., Azizi H., Stern R.J. & Asahara Y. 2023: The Sanandaj-Sirjan Zone (W. Iran) was a Jurassic passive continental margin: Evidence from igneous rocks of the Songhor area. *Lithos* 440, 107023. https://doi.org/10.1016/j.lithos.2023.107023

Nutman A.P., Mohajjel M., Bennett V.C. & Fergusson C.L. 2014: Gondwanan Eoarchean–Neoproterozoic ancient crustal material in Iran and Turkey: zircon U–Pb–Hf isotopic evidence. *Canadian Journal of Earth Sciences* 51, 272–285. https://doi.org/10.1139/cjes-2013-0138

Ondrejka M., Förster H.J., Bévan M., Uher P., Kianguebene-Koussingounina C.E. & Mahdy N.M. 2025: Evolution of accessory Nb–Ta–W–Sn–Ti–Fe oxide minerals from the Markersbach highly evolved aluminous A-type granite, Erzgebirge, Germany: Magmatic to hydrothermal processes and elemental mobility during F-rich fluid–rock interaction. *Geologica Carpathica* 76, 209–224. https://doi.org/10.31577/GeolCarp.2025.14

Passchier C.W. & Trouw R.A. 2005: *Microtectonics*. Springer, Berlin Heidelberg. https://doi.org/10.1007/3-540-29359-0

Pearce J.A., Harris N.B. & Tindle A.G. 1984: Trace element discrimination diagrams for the tectonic interpretation of granitic rocks. *Journal of Petrology* 25, 956–983. https://doi.org/10.1093/petrology/25.4.956

Qu X.-M., Wang R.-J., Xin H.-B., Jiang J.-H. & Chen H. 2012: Age and petrogenesis of A-type granites in the middle segment of the Bangonghu–Nujiang suture, Tibetan plateau. *Lithos* 146, 264–275. https://doi.org/10.1016/j.lithos.2012.05.006

Rubatto D. 2002: Zircon trace element geochemistry: partitioning with garnet and the link between U–Pb ages and metamorphism. *Chemical geology* 184, 123–138. https://doi.org/10.1016/S0009-2541(01)00355-2

Saccani E., Allahyari K., Beccaluva L. & Bianchini G. 2013: Geochemistry and petrology of the Kermanshah ophiolites (Iran): Implication for the interaction between passive rifting, oceanic accretion, and OIB-type components in the Southern Neo-Tethys Ocean. *Gondwana Research* 24, 392–411. https://doi.org/10.1016/j.gr.2012.10.009

Sahandi M., Radfar J., Hoseinidoust J. & Mohajjel M. 2006: *Geological map of Iran, 1/100000 series, sheet 5857*. Geological survey of Iran, Tehran.

Sepahi A.A. 2008: Typology and petrogenesis of granitic rocks in the Sanandaj-Sirjan metamorphic belt, Iran: with emphasis on the Alvand plutonic complex. *Neues Jahrbuch für Geologie und Paläontologie – Abhandlungen* 247, 295–312. https://doi.org/10.1127/0077-7749/2008/0247-0295

Sepahi A.A. & Athari S.F. 2006: Petrology of major granitic plutons of the northwestern part of the Sanandaj-Sirjan Metamorphic Belt, Zagros Orogen, Iran: with emphasis on A-type granitoids from the SE Saqqez area. *Neues Jahrbuch Fur Mineralogie – Abhandlungen* 183, 93–106. https://doi.org/10.1127/0077-7757/2006/0063

Shabanian N. & Neubauer F. 2024: From Early Jurassic intracontinental subduction to Early–Middle Jurassic slab break-off magmatism during the Cimmerian orogeny in the Sanandaj-Sirjan Zone, Iran. *Journal of Asian Earth Sciences* 267, 106153. https://doi.org/10.1016/j.jseaes.2024.106153

Shabanian N., Khalili M., Davoudian A. & Reza Mohajjel M. 2009: Petrography and geochemistry of mylonitic granite from Ghaleh-Dezh, NW Azna, Sanandaj-Sirjan zone, Iran. *Neues Jahrbuch für Mineralogie-Abhandlungen* 185, 233–248. https://doi.org/10.1127/0077-7757/2009/0121

Shabanian N., Davoudian A.R., Dong Y. & Liu X. 2018: U–Pb zircon dating, geochemistry and Sr-Nd-Pb isotopic ratios from Azna-Dorud Cadomian metagranites, Sanandaj-Sirjan zone of western Iran. *Precambrian Research* 306, 41–60. https://doi.org/10.1016/j.precamres.2017.12.037

Shabanian N., Davoudian A.R., Azizi H., Asahara Y., Neubauer F., Genser J., Dong Y. & Lee J.K. 2020: Petrogenesis of the Carboniferous Ghaleh-Dezh metagranite, Sanandaj–Sirjan zone, Iran: constraints from new zircon U–Pb and 40Ar/39Ar ages and Sr–Nd isotopes. *Geological Magazine* 157, 1823–1852. https://doi.org/10.1017/S0016756820000096

Shakerardakani F., Neubauer F., Masoudi F., Mehrabi B., Liu X., Dong Y., Mohajjel M., Monfaredi B. & Friedl G. 2015: Panafrican basement and Mesozoic gabbro in the Zagros orogenic belt in the Dorud–Azna region (NW Iran): laser-ablation ICP–MS zircon ages and geochemistry. *Tectonophysics* 647, 146–171. https://doi.org/10.1016/j.tecto.2015.02.020

Shakerardakani F., Neubauer F., Liu X., Dong Y., Monfaredi B. & Li X.-H. 2021: New detrital zircon U–Pb insights on the palaeogeographic origin of the central Sanandaj–Sirjan zone, Iran. *Geological Magazine* 158, 2165–2186. https://doi.org/10.1017/S0016756821000728

Sláma J., Košler J., Condon D.J., Crowley J.L., Gerdes A., Hanchar J.M., Horstwood M.S., Morris G.A., Nasdala L. & Norberg N. 2008: Plešovice zircon – a new natural reference material for U–Pb and Hf isotopic microanalysis. *Chemical geology* 249, 1–35. https://doi.org/10.1016/j.chemgeo.2007.11.005

Stipp M., Stünitz H., Heilbronner R. & Schmid S.M. 2002: Dynamic recrystallization of quartz: Correlation between natural and experimental conditions. *Geological Society, London, Special Publications* 200, 171–190. https://doi.org/10.1144/GSL.SP.2001.200.01.11

Stöcklin J. & Nabavi M. 1973: *Tectonic map of Iran, scale 1:2500000*. Geological Survey of Iran, Offset Press, Tehran.

Sun S.-S. & McDonough W.F. 1989: Chemical and isotopic systematics of oceanic basalts: implications for mantle composition and processes. *Geological Society, London, Special Publications* 42, 313–345. https://doi.org/https://doi.org/10.1144/GSL.SP.1989.042.01.19

Sylvester P.J. 1998: Post-collisional strongly peraluminous granites. *Lithos* 45, 29–44. https://doi.org/10.1016/S0024-4937(98)00024-3

Taylor S.R. & McLennan S.M. 1995: The geochemical evolution of the continental crust. *Reviews of Geophysics* 33, 241–265. https://doi.org/10.1029/95RG00262

Verschure R.H., Andriessen P.A.M., Boelrijk N.A.I.M., Hebeda E.H., Maijer C., Priem H.N.A. & Verdurmen E.T. 1980: On the thermal stability of Rb-Sr and K-Ar biotite systems: evidence from coexisting Sveconorwegian (ca 870 Ma) and Caledonian (ca 400 Ma) biotites in SW Norway. *Contributions to Mineralogy and Petrology* 74, 245–252. https://doi.org/10.1007/BF00371694

Wang L., Gao T., Li B. & Wang Y. 2024: Partial melting of amphibolite lower crust: A potential magma source for granite-related W mineralization. *Ore Geology Reviews* 167, 105978. https://doi.org/10.1016/j.oregeorev.2024.105978

Wang Z.Z., Teng F.Z., Zeng L. & Liu Z.C. 2024: Himalayan leucogranites: a geochemical perspective. *Elements* 20, 395–400. https://doi.org/10.2138/gselements.20.6.395

Warr L.N. 2021: IMA–CNMNC approved mineral symbols. *Mineralogical Magazine* 85, 291–320. https://doi.org/10.1180/mgm.2021.43

Whalen J.B., Currie K.L. & Chappell B.W. 1987: A-type granites: geochemical characteristics, discrimination and petrogenesis. *Contributions to Mineralogy and Petrology* 95, 407–419. https://doi.org/10.1007/BF00402202

Wiedenbeck M. 1995: An example of reverse discordance during ion microprobe zircon dating: an artifact of enhanced ion yields from a radiogenic labile Pb. *Chemical Geology* 125, 197–218.

Wiedenbeck M., Hanchar J.M., Peck W.H., Sylvester P., Valley J., Whitehouse M., Kronz A., Morishita Y., Nasdala L. & Fiebig J. 2004: Further characterisation of the 91500 zircon crystal. *Geostandards and Geoanalytical Research* 28, 9–39. https://doi.org/10.1111/j.1751-908X.2004.tb01041.x

Wilson M. 1989: Mid-ocean ridges. In: *Igneous petrogenesis*. Springer, 101–150. https://doi.org/10.1007/978-1-4020-6788-4_5

Electronic supplementary material is available online:

Supplementary Fig. S1 at https://geologicacarpathica.com/data/files/supplements/GC-77-6-Tahmasebi_FigS1.jpg
Supplementary Table S1 at https://geologicacarpathica.com/data/files/supplements/GC-77-6-Tahmasebi_TableS1.docx
Supplementary Tables S2–S6 at https://geologicacarpathica.com/data/files/supplements/GC-77-6-Tahmasebi_TablesS2-S6.docx
Supplementary Table S7 at https://geologicacarpathica.com/data/files/supplements/GC-77-6-Tahmasebi_TableS7.docx
Supplementary Table S8 at https://geologicacarpathica.com/data/files/supplements/GC-77-6-Tahmasebi_TableS8.docx